A Letters Journal Exploring the Frontiers of Physics

November 2013

EPL, **104** (2013) 40001
doi: 10.1209/0295-5075/104/40001

www.epljournal.org

Breather soliton solutions in a parametrically driven magnetic wire

D. Urzagasti[1], D. Laroze[1,2], M. G. Clerc[3] and H. Pleiner[2]

[1] *Instituto de Alta Investigación, Universidad de Tarapacá - Casilla 7D, Arica, Chile*
[2] *Max Planck Institute for Polymer Research - 55021 Mainz, Germany*
[3] *Departamento de Física, Facultad de Ciencias Físicas y Matemáticas, Universidad de Chile Casilla 4873, Santiago, Chile*

received 12 August 2013; accepted in final form 13 November 2013
published online 9 December 2013

PACS 05.45.Yv – Solitons
PACS 05.45.-a – Nonlinear dynamics and chaos
PACS 75.25.-j – Spin arrangements in magnetically ordered materials (including neutron and spin-polarized electron studies, synchrotron-source X-ray scattering, etc.)

Abstract – In the present work we study the pattern formation in a magnetic wire forced by a transversal uniform and oscillatory magnetic field. This system is described in the continuous framework by the Landau-Lifshitz-Gilbert equation. We find numerically that the spatio-temporal magnetization field exhibits a family of breather soliton states. We characterize different types of breathers as a function of the amplitude and frequency of the driven field.

Introduction. – Localized states have been observed in different fields, such as, chiral bubbles in liquid crystals, current filaments in gas discharge, spots in chemical reactions, localized states in fluid surface waves, oscillons in granular media, isolated states in thermal convection, solitary waves, just to mention a few [1,2]. In the framework of magnetism the classical localized solution is the soliton. The state of the art for conservative and for dissipative systems can be found in refs. [3–5]. Here, we deal with dissipative systems. Such systems can have spatially localized, stable, dynamic excitations [4]. Such a dynamic structure, appearing in a restricted spatial region and connecting asymptotically time-independent states in the rest of the space, are called dissipative solitons [1]. Such dissipative solitons in magnetic systems have been found, experimentally, [6,7]. In addition, magnetic solitonic modes in nano-oscillators have been observed [8–10]. Recently, dissipative magnetic droplet solitons were experimentally found and studied [11,12], after they were theoretically predicted in ref. [13]. In addition to ordinary single-soliton solutions, there exist other localized states [14–21]. In particular, there are complex time-dependent soliton states, called *breather solitons* [22–25]. The breathers are solitons such that their amplitude and width can vary on space and/or on time. This internal motion can be periodic, quasi-periodic or chaotic. Moreover, they were experimentally found in graphene nanoribbons [26], in chemical reactions [27], or in polymers [28]. Also, these states can be traveling or motionless in the space. Here we analyze the motionless dissipative breather solutions.

The aim of the present work is to investigate breather soliton precession states of an easy-plane ferromagnetic wire subject to a combined, constant and oscillatory, applied magnetic field. We perform intensive numerical simulations to characterize the region of existence of these localized solutions. In particular we focus on the dependence with the amplitude and the frequency of the external time-dependent magnetic field. We found that the number of oscillatory modes changes in a complex manner depending on these parameters. In fact, the oscillations can be periodic or quasi-periodic. Also, we found that the width and the amplitude of the soliton can be changed as a function of the parameters.

Theoretical model. – The standard approaches to study the dynamics of the macroscopic magnetization reversal are the Landau-Lifshitz equation, or the Landau-Lifshitz-Gilbert (LLG) equation [29]. These models have been used in both discrete [30–32] and continuous magnetic systems [16–20]. Let us consider a magnetic wire of total length L in the continuous framework, such that the normalized magnetization field is given by $\mathbf{m} = \mathbf{m}(\mathbf{r}, t)$, where $\mathbf{r}$ and t stand for the space coordinates and time, respectively. We focus on a ferromagnetic anisotropic long wire, so we consider the dynamics of the magnetization along the wire axis, represented by $\hat{\mathbf{z}} = (0, 0, 1)$. Hence,

the dynamical evolution of this wire can be modeled by the LLG equation and it can be written as

$$\frac{\partial \mathbf{m}}{\partial t} = -\mathbf{m}\times\mathbf{\Gamma} + \alpha\mathbf{m}\times\frac{\partial \mathbf{m}}{\partial t}. \qquad (1)$$

The effective torque field, $\mathbf{\Gamma}$, acting on the magnetization is given by $\mathbf{\Gamma} = \nabla^2\mathbf{m} - \beta(\mathbf{m}\cdot\hat{\mathbf{z}})\hat{\mathbf{z}} + \mathbf{h}$, where the Laplacian term accounts for the coupling of the magnetization with the first neighbors, $\beta \geq 0$ measures the anisotropy along the $\hat{\mathbf{z}}$-axis, and $\mathbf{h}$ is the external magnetic field. In this case the LLG equation is invariant under the rescaling $\alpha = \eta\,\alpha'$, $\beta = \sigma\,\beta'$, $\mathbf{m} = \mathbf{m}'/\eta$, $t = \eta\,t'/\sigma$, $z = z'/\sqrt{\sigma}$, $\mathbf{h} = \sigma\,\mathbf{h}'/\eta$, for $\eta > 0$ and $\sigma > 0$.

Let us take into account an external magnetic field that comprises both a constant and an oscillatory part, $\mathbf{h} = (h_c + h_0\cos(\Omega t))\hat{\mathbf{x}}$, where the coefficients $\{h_c, h_0, \Omega\}$ are constants. Here α denotes the dimensionless phenomenological damping coefficient which is a material property. Throughout this manuscript we use dimensionless quantities having scaled the magnetization (and magnetic fields) by the saturation magnetization M_S; the time t by $1/\gamma_0 M_S$, where $\gamma_0 = 2.2\times10^5\,\mathrm{A^{-1}ms^{-1}}$ is the electron gyromagnetic ratio [29], and the space coordinates $\mathbf{r}$ by the exchange length $\ell_{ex} = \sqrt{2A/\mu_0 M_S^2}$, where A is the exchange stiffness constant. In the long-wire approximation, the dimensionless anisotropy parameter becomes $\beta = -(1/2 + 2K_u/\mu_0 M_S^2)$, where K_u is the uniaxial anisotropy constant and the $1/2$ term corresponds to the dipole field contribution [33]. Taking, *e.g.*, material values for $CsNiF_3$ [34–36]: $M_s = 2.2\times10^5\,\mathrm{A/m}$, $K_u = -1.2\times10^6\,\mathrm{J/m^3}$, $A = 0.8\,\mathrm{pJ/m}$, we obtain $\ell_{ex} = 5\,\mathrm{nm}$, $\tau = 20\,\mathrm{ps}$, and that $\beta = 39$.

In the macro-spin approximation, when spatial coupling is ignored, the system can exhibit uniform states, periodic solutions, quasi-periodic solutions, or chaotic states depending on the parameters [30–32]. In this approximation a simple homogeneous state of model (1) is $\mathbf{m} = \hat{\mathbf{x}}$, which represents a uniform magnetization parallel to the magnetic forcing. Small perturbations of this homogeneous state are characterized by damped dispersive oscillations, with frequencies close to $\Omega_0 = \sqrt{h_c(h_c+\beta)}$. When the wire is forced at about twice this natural frequency, $\Omega \equiv 2(\Omega_0 + \nu)$, ν being the detuning parameter, this uniform state becomes unstable by means of an oscillatory instability. This subharmonic bifurcation is characterized by a (complex) Floquet multiplier that crosses the unit cycle at -1. This bifurcation gives rise to a uniform attractive periodic solution, which corresponds to a parametric resonance [20]. More precisely, the bifurcation occurs at $h_{0,c}^2 = (4\Omega_0)^2[\nu^2 + (\alpha q/2)^2]/\beta^2$ with $q = \beta + 2h_c$; this relationship defines the first Arnold tongue.

The inclusion of spatial couplings, which in our case is represented by the Laplacian term, should increase the complexity of the dynamical behavior. For example, one expects the formation of standard dissipative soliton solutions [4,5], two-soliton solutions [16], domain walls, and localized states near the parametric resonance [17–21]. Apart from the standard soliton solution, we numerically found other types of localized structures by directly solving eq. (1). In particular, the system exhibits a stable breather soliton solutions, where the localized dynamic structure exhibits an internal spatio-temporal modulation. Figure 1 shows the second component of the magnetization field, $m_y(z,t)$, as a function of space and time for the standard soliton states (panel (a)) and two breather soliton states with different types of internal modulations (panels (b) and (c)). The fast Fourier transforms (FFT) of the central points of the breather solitons of panels (b) and (c) are shown in fig. 2, revealing the temporal

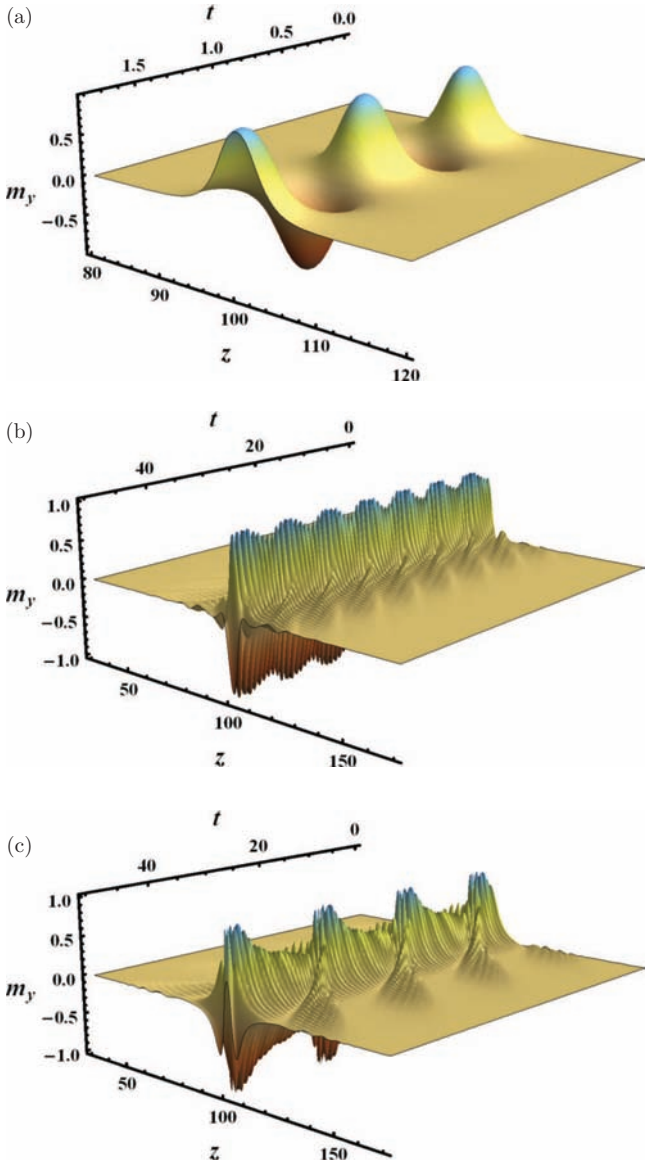

Fig. 1: (Color online) y-component of the magnetization, $m_y(t,z)$, as a function of the space and time for different values of ν and h_0 at $\alpha = 0.015$, $h_c = 3$, $\beta = 20$. In panels (a)–(c) the values of the pair (h_0, ν) are $(0.476, -0.302)$, $(0.578, -0.390)$, $(0.732, -0.495)$, respectively.

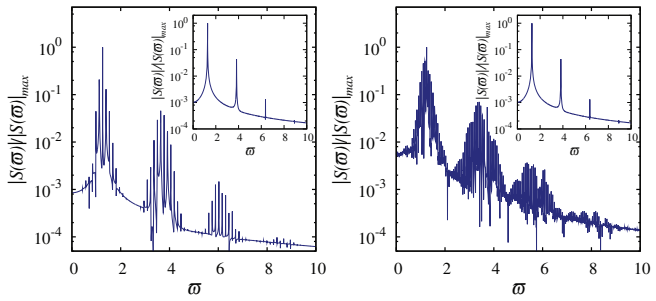

Fig. 2: (Color online) Fourier power spectrum of the central point of $m_y(t,z)$ for the breather-soliton–like solutions appearing in panels (b) and (c) of fig. 1. The inset in both panels is the corresponding Fourier power spectrum of the simple soliton solution given in panel (a) of fig. 1.

complexity. In fact, we can observe that, instead of the (four) single peaks of the standard soliton, these new states show (four) peaked distributions of multiple peaks. Hence, a breather soliton solution is exhibited when a splitting in the four original peaks is observed. Since the fourth peak is small with respect to the others, we will only analyze the three first ones in the following. The complete details of the simulations and the corresponding characterization are given in the next section.

Simulations. – Firstly, let us describe the numerical method. We have numerically solved eq. (1) using the variable step fifth-order Runge-Kutta (RK) scheme with a maximum tolerance of $10^{-5}\%$, over a linear lattice of size 5×10^2 a.u. with a spatial discretization step set to 0.4. We use a double-precision RK method provided in ref. [37]. In order to test our numerical scheme we have monitored step by step the dynamical constraint, $|\mathbf{m}(z,t)|^2 = 1$, with a precision of 10^{-6}, which is sufficiently small for the purpose of the present analysis. For comparison we have also studied smaller and larger lattice sizes and discretization steps to guarantee that there are no finite-size effects. We have integrated the system for the time interval $t_F = 5\times10^3$, which is almost four times the transient time and seems to be long enough. The fixed parameters in the simulations are $\{\alpha,\beta,h_c\} = \{0.015, 20, 3\}$, which applies to $CsNiF_3$ taking $\sigma = 0.51$ and $\eta \leq 1$.

Dynamical indicators. For the temporal analysis of each solution we first take the FFT of the central point (at $z_0 = L/2$) of the y-component of the magnetization, FFT $(m_y(t,z_0))$, which gives us a complex discrete signal, $S(\varpi)$, in frequency space $\varpi = (\varpi_1,\ldots,\varpi_n)$, producing a set of pairs $\{\varpi_k, S(\varpi_k)\}$. For this signal we calculate its power spectrum $|S(\varpi)|^2$ and count the numbers of peaks, N_ϖ, corresponding to a given frequency, which is a measure for the number of oscillation modes. We have defined a peak when its height relative to the background is greater than 10^{-7}. We start the FFT calculation at $t_0 = 4.8\times10^3$ within a rectangular time window of $\Delta t = 200$, and with 2^{16} sample points.

In addition, we calculate the probability to obtain a state with frequency ϖ_q,

$$P_q = |S(\varpi_q)|^2 \left[\sum_{j=1}^{N_\varpi} |S(\varpi_j)|^2\right]^{-1}, \tag{2}$$

which gives us the information about the predominant frequencies in the modulation.

Moreover, in order to obtain a global characterization, we have calculated the magnetic energy of the system [29]

$$Q = \frac{1}{L}\int_0^L \mathrm{d}z \left[\frac{1}{2}(\partial_z \mathbf{m})^2 - \frac{\beta}{2}(1-m_z^2) - \mathbf{h}\cdot\mathbf{m}\right], \tag{3}$$

which is frequently used as an indicator to detect non-regular dynamics in optics, localized patterns in fluids, and other physical systems [2]. We remark that the time dependence of Q reflects the temporal behavior of the patterns, *i.e.* in a stationary regime, Q is constant, while in a (quasi-)periodic one, Q is a (quasi-)periodic function of time. Consequently, if the system is in a chaotic regime, the time series of Q will also be chaotic. Taking the maximum value of Q within a fixed time interval, one can generate a bifurcation diagram as a function of the parameters.

To complement the information (in particular to discriminate between quasi-periodic and chaotic dynamics) and to provide a more quantitative aspect of the dynamics, we calculate the largest Lyapunov exponent [38], defined by

$$\lambda_{max} = \lim_{t\to\infty} \frac{1}{t} \ln \frac{\|\delta\mathbf{m}(t,z)\|}{\|\delta\mathbf{m}(t_0,z)\|}, \tag{4}$$

where $\|\bullet\| \equiv (\int_0^L \mathrm{d}z |\bullet|^2)^{1/2}$ and $\delta\mathbf{m}$ satisfies the differential equation

$$\frac{\partial\delta\mathbf{m}}{\partial t} = \bar{\mathbf{J}}\cdot\delta\mathbf{m}, \tag{5}$$

with $\bar{\mathbf{J}}$ the Jacobian matrix of eq. (1) with respect to $\mathbf{m}$. This number quantifies how fast the distance, $\delta\mathbf{m}$, between two initially close trajectories (one of them called the *fiducial* trajectory) of the vector field $\mathbf{m}$ either vanishes ($\lambda_{max} < 0$) or diverges exponentially ($\lambda_{max} > 0$). The latter is the hallmark of chaotic behavior. We calculate λ_{max} from $t_0 = 4.8\times10^3$ up to $t_{max} = 14.4\times10^3$. In order to overcome exponential divergences we rescale $\|\delta\mathbf{m}(t,z)\|$ by the initial norm $\|\delta\mathbf{m}(t_0,z)\|$ and take as time steps $\Delta t = 1.5625$.

For the spatial analysis we compute the space-time average of the width of the solitons, Δ_a, which we define as

$$\Delta_a^2 = \frac{2^2}{L\zeta}\int_0^L \mathrm{d}z \left(z - \left(\frac{1}{L\zeta}\int_0^L \mathrm{d}z' z' \Lambda_a(z')\right)\right)^2 \Lambda_a(z), \tag{6}$$

where

$$\zeta = \frac{1}{L}\int_0^L \mathrm{d}z\, \Lambda_a(z), \tag{7}$$

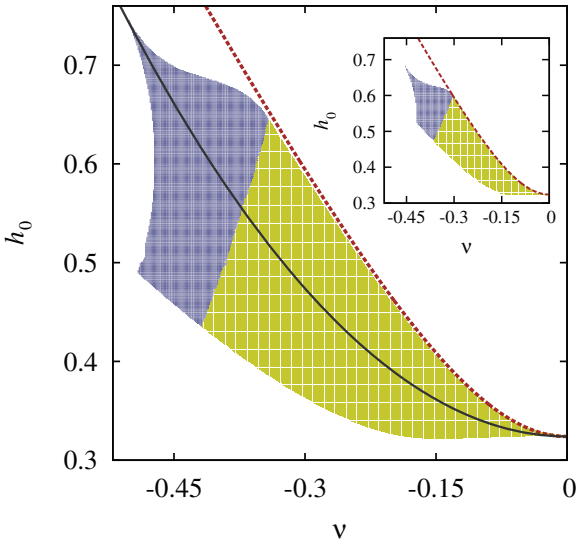

Fig. 3: (Color online) The existence range of solitons in the h_0 (field amplitude), and ν (detuning parameter) phase diagram of eq. (1) and eq. (8) (inset) for $\alpha = 0.015$, $h_c = 3$, and $\beta = 20$. The (green) squares denote single-soliton solutions, while filled (blue) circles represent the breather soliton states. The dashed line is the first Arnold tongue, while the (continuous) parabola, $h_0(\nu_{h_0}) = 1.665\,\nu_{h_0}^2 + 0.324$, is used in the following as a reference curve to show the different behavior.

and $\Lambda_j(z) = \sqrt{\langle(\delta_{jx} - m_j(z,t))^2\rangle}$, with $j \in \{x, y, z\}$; δ_{ab} being the Kronecker-Delta distribution and $\langle\bullet\rangle$ denoting the time average. This particular choice for the weight function is adopted because we consider perturbations to the homogeneous state $\mathbf{m} = \hat{\mathbf{x}}$.

Numerical results. The existence region of dissipative breather solitons is shown in fig. 3. This phase diagram contains the spatio-temporal evolution of 5.4×10^4 points in the ν-h_0 parameter space. The standard solitons and breathers are denoted by squares (green) and circles (blue), respectively. We observe that the existence range of standard solitons is larger than that of the breathers, and the latter occur for more negative detuning values. In order to build this phase diagram, we start with the same initial condition and determine the final state for various values of ν and h_0. For this initial condition we always take a soliton-shaped profile with the bump located in the center of the wire, explicitly given by $m_y(z,0) = m_{y0} = \mathrm{sech}(z - z_0)/2$, $m_z(z,0) = f\,m_{y0}$ and $m_x(z,0) = [1 - (1+f^2)\,m_{y0}^2]^{1/2}$, where $f = 0.95$ and $z_0 = 10^2$. Depending on the parameters, this perturbation either decays (no soliton), evolves as a single soliton, or forms an extended pattern. The existence range of these solutions is robust against starting with different finite amplitude initial conditions. Nevertheless, starting with a gas of solitons as initial condition, the system could additionally exhibit bound soliton states [16].

Figure 3 also shows the parabola $h_0(\nu_{h_0}) = 1.665\,\nu_{h_0}^2 + 0.324$, along which we discuss the sequence of different dynamical states in fig. 4. There, the final states of the y-component of the magnetization, $m_y(z, t = t_F)$, along the curve $h_0(\nu_{h_0})$, is shown in arbitrary units (according to the attached color code). From bottom to top we observe standard solitons, breather solitons, extended patterns, and homogeneous solutions. While standard solitons have a well-defined spatial width, breather solitons radiate waves that propagate laterally, where they fade away. Following the same curve, there is a critical value of the detuning parameter, for which the dynamics changes abruptly to a regime with patterns that are not localized, but fill the entire wire. Above that regime there is a sharp transition to a soliton-free area in phase space.

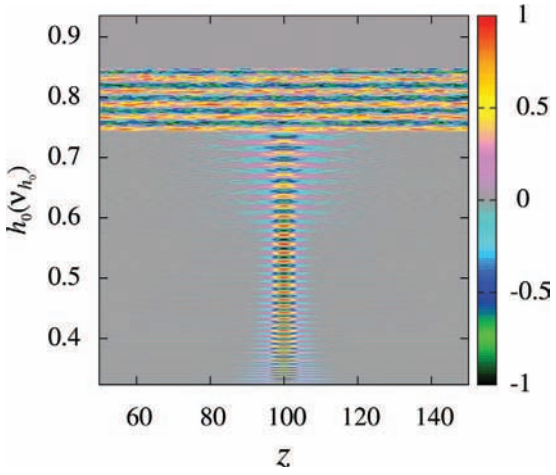

Fig. 4: (Color online) Final states of the y-component of the magnetization, $m_y(z, t = t_F)$, (in a.u.) along the continuous reference curve in fig. 3. From bottom to top there are standard solitons, breather solitons, extended patterns, and homogeneous solutions.

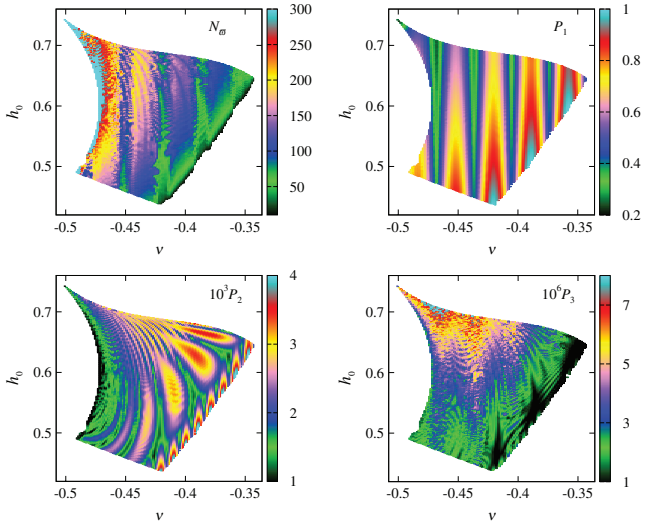

Fig. 5: (Color online) Number of oscillation modes, N_ϖ, (top left) and the probabilities associated with the first three breather soliton frequencies (in a.u.). Notice the different scales used for $P_{1,2,3}$.

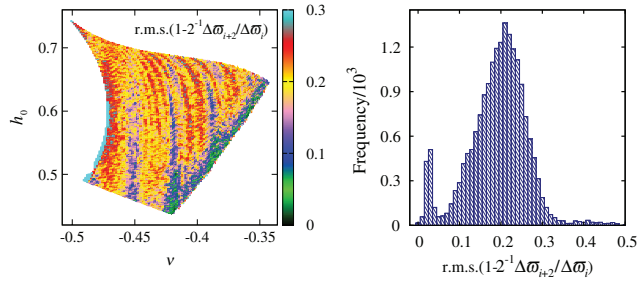

Fig. 6: (Color online) The map of the r.m.s. deviations from unity of the distance ratio $2^{-1}\Delta\varpi_{i+2}/\Delta\varpi_i$ (left) and its histogram (right) for adjacent peaks in the spectra of breather solitons.

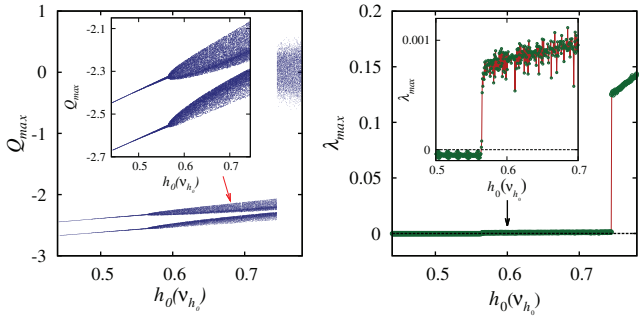

Fig. 7: (Color online) Bifurcation diagram using the maxima of the magnetic energy, Q, and the maximum Lyapunov exponent along the continuous parabola $h_0(\nu_{h_0})$ shown in fig. 3.

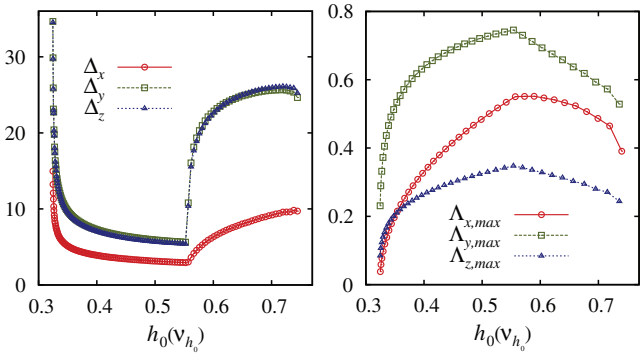

Fig. 8: (Color online) Average width and average maximum amplitude of the components of $\mathbf{m}$ along the continuous reference curve in fig. 3.

Figure 5 shows, in the ν-h_0 phase space, the number of FFT modes, N_ϖ, (upper left panel) and the corresponding three probabilities, $\{P_1, P_2, P_3\}$ associated with the first three soliton frequencies. The number of modes has a complicated and non-monotonous dependence on h_0 and ν, although there is an overall tendency to find the highest (lowest) numbers of modes for the most (least) negative values of ν. Similarly, all probabilities, $\{P_j\}$, show a structured behavior (rather than being monotonous) in this phase-space projection. For example, we can distinguish a fold-like pattern for P_1, globular-type patterns for P_2, and a kind of curved stripes for P_3. Generally, the probabilities P_j decay rapidly with increasing number j, $P_1 \gg P_2 \gg P_3$.

Let us analyze in more detail the Fourier spectra in order to clarify, whether breather solitons are (multi-)periodic or quasi-periodic solitons. If the localized states are periodic, there exists a gap $\Delta\varpi_{min}$ such that all distances between the various peaks in a given spectrum, $\Delta\varpi$, are an integer (K) multiple of the minimal one, $\Delta\varpi = K\,\Delta\varpi_{min}$. Hence, for $(n+1)$-adjacent peaks with $\Delta\varpi_{i+n} = \varpi_{i+n} - \varpi_i$ there is $n^{-1}\Delta\varpi_{i+n}/\Delta\varpi_i = 1$ for periodic spectra, and $\neq 1$ for quasi-periodic ones. For each spectrum from the sample of about 1.9×10^4 spectra of breather solitons we calculate the r.m.s. deviation from the unity of the distance ratio $2^{-1}\Delta\varpi_{i+2}/\Delta\varpi_i$ (fig. 6 (left)), and build the corresponding histogram (fig. 6 (right)). These results, with a few exceptions ($\sim$0.1%), show an appreciable departure from unity, demonstrated in the histogram by the broad peak at a finite value, and therefore prove quasi-periodicity for breather solitons.

Figure 7 shows the bifurcation diagram in terms of Q and the largest Lyapunov exponent, λ_{max}, along the curve $h_0(\nu_{h_0})$. The magnetic energy Q shows two branches corresponding to the two most important oscillation frequencies. There is a dramatic change in the dynamics (enhanced in the inset) from standard soliton to breather soliton states when the value of $h_0(\nu_{h_0})$ is increased (beyond ca. 0.563). Increasing the value of $h_0(\nu_{h_0})$ further (beyond ca. 0.744) the system suffers another abrupt instability to the extended pattern state. This part of the bifurcation diagram is of the typical chaotic type. To complement this analysis the largest Lyapunov exponent is shown in the right frame of fig. 7. Since all the values of λ_{max} are clearly positive in the extended pattern states, we conclude that these states are chaotic. In the range of the ordinary soliton solutions, λ_{max} is negative indicating non-chaotic behavior. The transition from the standard to the breather solitons is clearly visible in the inset and λ_{max} jumps from a slightly negative value to a slightly positive one. In principle, this signals chaos, but the value of λ_{max} is so small that it might be compatible with zero within the numerical accuracy. In that case it fits to the quasi-periodic interpretation of the bias from unity evidenced in the distribution of fig. 6. Certainly, the spatio-temporal behavior of the breathers is rather complex.

In addition, we want to compare the spatial "form" of ordinary and breather solitons. Figure 8 shows the average spatial width and the average maximum amplitude of the three components of $\mathbf{m}$ along the curve $h_0(\nu_{h_0})$. The abrupt transition from standard to breather solitons is obvious and manifest by kink-like features. Nevertheless, both types of solitons become taller and narrower towards the transition zone.

Finally, let us comment that a simpler description of these soliton states can be given by an amplitude equation of the envelope of the z-component of $\mathbf{m}$ ($m_z \propto \mathrm{Re}(A\exp(i(\Omega_0+\nu)t)+\ldots)$, where the complex amplitude

A satisfies

$$\partial_t A = -(i\nu + \mu)A - iA|A|^2 + \gamma\bar{A} - i\partial_Z^2 A, \qquad (8)$$

with $\mu = \alpha q/2$, $\gamma = \beta h_0/4\Omega_0$ and $Z = \sqrt{2\Omega_0/q}\, z$. The last equation is known as the *parametrically driven, damped nonlinear Schrödinger equation* (PDDNLS) [4,5]. We solve numerically eq. (8) and found that the standard and the breather solitons have a phase diagram which is qualitatively similar to the LLG diagram as is shown in the inset of fig. 3. In general, amplitude equations give a qualitatively correct description, although often quantitative agreement is not obtained [5]. More details about breathers in the PDDNLS can be found in refs. [23–25].

Final remarks. – In summary, we have determined the parameter region where dissipative breather soliton precession states occur in an anisotropic magnetic wire exposed simultaneously to a constant and a time-dependent magnetic field. We found that depending on the amplitude and the frequency of the driven field the numbers of oscillatory modes change from several modes up to hundreds of modes, and the probabilities to find a specific mode of the Fourier spectra have intricate patterns. Bifurcation diagrams using the maxima of the magnetic energy and the calculation of the largest Lyapunov exponent have allowed us to conclude that breather solitons in the system under study are not chaotic states. Furthermore, using the peaks in the Fourier spectra, we numerically prove that their frequencies are incommensurable, indicating that breather solitons are quasi-periodic localized patterns. Finally, we remark that we have also obtained dissipative breather solitons in the case of negative β, applicable to, *e.g.*, $Ni_{80}Fe_{20}$ [9,10]. The complete characterization of those localized structures is still in progress.

* * *

The authors acknowledge partial financial support from UTA-project 8750-12, CEDENNA, and Millennium Scientific Initiative, P10-061-F. DU acknowledges the PhD program fellowship through the Performance Agreement Project's UTA/Mineduc.

REFERENCES

[1] Descalzi O. *et al.* (Editors), *Localized States in Physics: Solitons and Patterns* (Springer, Berlin) 2010.
[2] Ankiewics A. and Akhmediev N. (Editors), *Dissipative Solitons: From Optics to Biology and Medicine* (Springer, Berlin) 2008.
[3] Kosevich A. M., Ivanov W. A. and Kovalev A. S., *Phys. Rep.*, **194** (1990) 117.
[4] Barashenkov I. V., Bogdan M. M. and Korobov V. I., *Europhys. Lett.*, **15** (1991) 113.
[5] Clerc M. G., Coulibaly S. and Laroze D., *EPL*, **90** (2010) 38005.
[6] Wang Z. *et al.*, *Phys. Rev. Lett.*, **107** (2011) 114102.
[7] Ustinov A. B. *et al.*, *Phys. Rev. Lett*, **106** (2011) 017201.
[8] Slavin A. and Tiberkevich V., *Phys. Rev. Lett.*, **95** (2005) 237201.
[9] Bonetti S. *et al.*, *Phys. Rev. Lett.*, **105** (2010) 217204.
[10] Dumas R. K. *et al.*, *Phys. Rev. Lett.*, **110** (2013) 257202.
[11] Mohseni S. M. *et al.*, *Science*, **339** (2013) 1295.
[12] Iacocca E. *et al.*, arXiv:1308.4812v1 (2013).
[13] Hoefer M. A., Silva T. J. and Keller M. W., *Phys. Rev. B*, **82** (2010) 054432.
[14] Barashenkov I. V., Woodford S. R. and Zemlyanaya E. V., *Phys. Rev. E*, **75** (2007) 026604.
[15] Janutka A., *Phys. Pol. A*, **124** (2013) 23.
[16] Urzagasti D. *et al.*, *J. App. Phys.*, **111** (2012) 07D111.
[17] Clerc M. G., Coulibaly S. and Laroze D., *Phys. Rev. E*, **77** (2008) 056209.
[18] Clerc M. G., Coulibaly S. and Laroze D., *Int. J. Bifurcat. Chaos*, **19** (2009) 2717.
[19] Clerc M. G., Coulibaly S. and Laroze D., *Int. J. Bifurcat. Chaos*, **19** (2009) 3525.
[20] Clerc M. G., Coulibaly S. and Laroze D., *Physica D*, **239** (2010) 72.
[21] Clerc M. G., Coulibaly S. and Laroze D., *EPL*, **97** (2012) 30006.
[22] Bondila M., Barashenkov I. V. and Bogdan M. M., *Physica D*, **87** (1995) 314.
[23] Barashenkov I. V. and Zemlyanaya E. V., *Phys. Rev. E*, **83** (2011) 056610.
[24] Barashenkov I. V., Zemlyanaya E. V. and van Heerden T. C., *Phys. Rev. E*, **83** (2011) 056609.
[25] Alexeeva N. V. and Zemlyanaya E. V., *Theor. Math. Phys.*, **168** (2011) 858.
[26] Savin V. and Kivshar Y. S., *Phys. Rev. B*, **81** (2010) 165418.
[27] Maniadis P. *et al.*, *Phys. Rev. E*, **60** (1999) 7618.
[28] Teramoto T., Wang Z. and Kobryanskii V. M., *Phys. Rev. B*, **79** (2009) 033202.
[29] Mayergoyz I. D., Bertotti G. and Serpico C., *Nonlinear Magnetization Dynamics in Nanosystems* (Elsevier, Oxford, UK) 2009.
[30] Laroze D. *et al.*, *IEEE Trans. Magn.*, **47** (2011) 3032.
[31] Bragard J. *et al.*, *Phys. Rev. E*, **84** (2011) 037202.
[32] Laroze D. *et al.*, *IEEE Trans. Magn.*, **48** (2012) 3567.
[33] Cullity B. D. and Graham C. D., *Introduction to Magnetic Materials* (Wiley, Hoboken, USA) 2009.
[34] Delica T. *et al.*, *Phys. Rev. B*, **44** (1991) 11773.
[35] Schmidt R. E. *et al.*, *Z. Anorg. Allg. Chem.*, **625** (1999) 637.
[36] Trudeau Y. and Plumer M. L., *Phys. Rev. B*, **51** (1995) 5868.
[37] Press W. H. *et al.*, *Numerical Recipes in FORTRAN* (Cambridge University Press, Cambridge, UK) 1992.
[38] Wolf A. *et al.*, *Physica D*, **16** (1985) 285.